A Double-Sided LCC Compensation Network and Its Tuning Method for Wireless Power Transfer

Siqi Li, *Member, IEEE*, Weihan Li, *Student Member, IEEE*, Junjun Deng, *Student Member, IEEE*, Trong Duy Nguyen, *Member, IEEE*, and Chunting Chris Mi, *Fellow, IEEE*

***Abstract*—This paper proposes a double-sided LCC compensation network and its tuning method for wireless power transfer (WPT). With the proposed topology and its tuning method, the resonant frequency is irrelevant with the coupling coefficient between the two coils and is also independent of the load condition, which means that the system can work at a constant switching frequency. Analysis in frequency domain is given to show the characteristics of the proposed method. We also propose a method to tune the network to realize zero voltage switching (ZVS) for the Primary-side switches. Simulation and experimental results verified analysis and validity of the proposed compensation network and the tuning method. A wireless charging system with output power of up to 7.7 kW for electric vehicles was built, and 96% efficiency from dc power source to battery load is achieved.**

***Index Terms*—Battery charger, current source, electric vehicle, wireless power transfer (WPT), zero voltage switching (ZVS).**

NOMENCLATURE

$S_1 \sim S_4$	Primary-side MOSFETs.
$D_1 \sim D_4$	Secondary-side rectifier diodes.
L_1	Self-inductance of the transmitting coil.
L_{f1}	Primary-side compensation inductance.
L_2	Self-inductance of the receiving coil.
L_{f2}	Secondary-side compensation inductance.
L_{s1}	Leakage inductance of the transmitting coil.
L_{s2}	Leakage inductance of the receiving coil.
L_m	Magnetizing inductance referred to the primary side.
L'_{f2}	Converted secondary-side compensation inductance referred to the primary side.
L_{e1}	Equivalent inductance of the primary-side series capacitor and leakage inductance.
L'_{e2}	Converted equivalent inductance of the secondary-side series capacitor and leakage inductance referred to the primary side.
ΔL_{e2}	Decrement of the equivalent inductance of secondary-side series capacitor and leakage inductance.
$\Delta L'_{e2}$	Converted decrement of the equivalent inductance of the secondary-side series capacitor and leakage inductance referred to the primary side.
C_1	Primary-side series compensation capacitor.
C_{f1}	Primary-side parallel compensation capacitor.
C_2	Secondary-side series compensation capacitor.
C_{f2}	Secondary-side parallel compensation capacitor.
C'_2	Converted secondary-side series compensation capacitor referred to the primary side.
C'_{f2}	Converted secondary-side parallel compensation capacitor referred to the primary side.
ΔC_2	Increment of the secondary-side series compensation capacitor.
M	Mutual inductance between the transmitting and receiving coils.
k	Coupling coefficient between the transmitting and receiving coils.
n	Equivalent turns ratio between the transmitting and receiving coils.
ω_0	Resonant angular frequency.
$\mathbf{U}_{AB}$	Phasor of the first-order input voltage applied on the primary side.
U_{AB}	First-order rms value of the input voltage.
$\mathbf{U}_{AB\_m\text{th}}$	Phasor of the mth-order input voltage.
u_{ab}	The square-wave output voltage of the secondary side before the rectifier.
$\mathbf{U}_{ab}$	Phasor of the first-order output voltage before the rectifier.
U_{ab}	First-order rms value of the output voltage before the rectifier.
$U_{ab\_\min}$	Minimum rms value of the output voltage before the rectifier.
$\mathbf{U}'_{ab}$	Phasor of the first-order output voltage referred to the primary side.

Manuscript received December 16, 2013; revised May 10, 2014 and July 1, 2014; accepted July 30, 2014. Date of publication August 12, 2014; date of current version June 16, 2015. This work was supported in part by the U.S. Department of Energy under an Energy Graduate Automotive Technology Education Grant, by the U.S.–China Clean Energy Research Center-Clean Vehicle Consortium, DENSO International, by the University of Michigan, and by the China Scholarship Council. The review of this paper was coordinated by Prof. A. Khaligh.

S. Li is with the Department of Electrical and Computer Engineering, University of Michigan, Dearborn, MI 48128 USA, and also with the Department of Electrical Engineering, Kunming University of Science and Technology, Kunming 650500, China (e-mail: lisiqi00@gmail.com).

W. Li is with the Department of Electrical and Computer Engineering, University of Michigan, Dearborn, MI 48128 USA, and also with the Department of Mechanical and Automotive Engineering, Hefei University of Technology, Hefei 230009, China (e-mail: weihanli1988@gmail.com).

J. Deng is with the Department of Electrical and Computer Engineering, University of Michigan, Dearborn, MI 48128 USA, and also with the Department of Electrical Engineering, Northwestern Polytechnical University, Xi'an 710072, China (e-mail: dengjunjun1985@gmail.com).

T. D. Nguyen and C. C. Mi are with the Department of Electrical and Computer Engineering, University of Michigan, Dearborn, MI 48128 USA (e-mail: ntrduy@gmail.com; chrismi@umich.edu).

Color versions of one or more of the figures in this paper are available online at http://ieeexplore.ieee.org.

Digital Object Identifier 10.1109/TVT.2014.2347006

$\mathbf{U}_{ab\_m\text{th}}$	Phasor of the mth-order output voltage before rectifier.
$\mathbf{I}_{Lf1}$	Phasor of the current on the primary-side compensation inductor L_{f1}.
$\mathbf{I}_1$	Phasor of the current on the transmitting coil.
$\mathbf{I}_2$	Phasor of the current on the receiving coil.
$\mathbf{I}'_2$	Phasor of the current on the receiving coil referred to the primary side.
$\mathbf{I}_{Lf2}$	Phasor of the current on the secondary-side compensation inductor L_{f2}.
$\mathbf{I}'_{Lf2}$	Phasor of the current on L_{f2} referred to the primary side.
$\mathbf{I}_{Lf1AB}$	Phasor of the current on L_{f1} when only $\mathbf{U}_{AB}$ is applied.
$\mathbf{I}_{1AB}$	Phasor of the current on the transmitting coil when only $\mathbf{U}_{AB}$ is applied.
$\mathbf{I}'_{2AB}$	Phasor of the current on the receiving coil when $\mathbf{U}_{AB}$ applied only referred to the primary side.
$\mathbf{I}'_{Lf2AB}$	Phasor of the current on L_{f2} when $\mathbf{U}_{AB}$ applied only referred to the primary side.
$\mathbf{I}_{1ab}$	Phasor of the current on the transmitting coil when only $\mathbf{U}_{ab}$ is applied.
$\mathbf{I}'_{2ab}$	Phasor of the current on the receiving coil when $\mathbf{U}_{ab}$ applied only referred to the primary side.
$\mathbf{I}'_{Lf2ab}$	Phasor of the current on L_{f2} when $\mathbf{U}_{ab}$ applied only referred to the primary side.
$\mathbf{I}_{Lf1\_m\text{th}}$	Phasor of the mth order current on L_{f1}.
$\mathbf{I}_{Lf1ab\_1\text{st}}$	Phasor of the first-order current on L_{f1} when only $\mathbf{U}_{ab}$ is applied.
$\mathbf{I}_{Lf2\_m\text{th}}$	The phasor of the mth order current on L_{f2}.
I_{OFF}	Turn-off current of the MOSFETs.
$I_{\text{OFF\_min}}$	Minimum turn-off current of the MOSFETs.
φ	Phase by which $\mathbf{U}_{ab}$ leads $\mathbf{U}_{AB}$.
φ_1	Phase by which $\mathbf{I}_{Lf2\_1\text{st}}$ leads $\mathbf{U}_{AB}$.
φ_2	Phase by which $\mathbf{U}_{ab}$ leads $\mathbf{I}_{Lf2\_1\text{st}}$.
U_{in}	The dc input voltage.
U_b	Battery voltage.

I. Introduction

WIRELESS power transfer (WPT) using magnetic resonant concept was proposed by Nikola Tesla more than 100 years ago. Until recently, with the development of power electronics technology, it is realized that a WPT system can be implemented economically enough to have a commercial value. Several companies, such as WiTricity, Evatran, Qualcomm, etc., have already developed a few products that can transfer power with acceptable power level and efficiency through a certain air gap. A lot of new research, such as the amazing 2-m 60-W power transfer [1], various analysis and control methods [2]–[5], and the guided power transfer path using the domino-form repeaters [6], [7], have also been published lately.

In a WPT system, the energy is transferred through the mutual inductance of the transmitting and receiving coils, whereas the leakage inductance does not have a direct contribution to the active power transfer. Because of the large gap between the transmitting and receiving coils, the coupling coefficient between the two coils is small, i.e., typically in the range of 5%–30% depending on the distance, alignment, and size of the coils. This causes the WPT systems to have a large leakage inductance but a small mutual inductance. To increase the coupling, the coil design, without a doubt, is important [8]. Meanwhile, the compensation circuit, which is used to cancel the leakage inductance, is also of great importance. Usually, capacitors, which can be lumped or parasitic, are added to form a resonant circuit, which is known as the magnetic resonant method.

Different compensation topologies have been proposed and implemented to tune the two coils working at a resonant frequency in a wide range of applications. There are four basic topologies depending on how the compensation capacitors are added to the transmitting and receiving coils, namely, series–series (SS), series–parallel, parallel–series, and parallel–parallel topologies [9], [10]. Some other novel topologies have also been proposed in the literature. In [11], a dual topology is realized by switching between a parallel-compensated secondary side and a series-compensated secondary side to realize both constant current mode and constant voltage mode. Moreover, the transmitting and receiving coils need to be connected to the power electronics converters. To achieve high efficiency for the complete WPT system, some other superior topologies have been proposed. In [12], an LCL converter is formed by adding LC compensation network between the converter and the transmitting coil. There are two advantages for the LCL converter when the system works at the resonant frequency. First, the inverter only supplies the active power required by the load; second, the current in the primary-side coil is independent of the load condition. In [13], an LC compensation network at both primary and secondary sides is proposed for bidirectional power transfer. The design of an LCL converter usually requires the same value for the two inductors. To reduce the additional inductor size and cost, usually, a capacitor is put in series with the primary-side coil, which forms an LCC compensation network. By utilizing an LCC compensation network, a zero current switching (ZCS) condition could be achieved by tuning the compensation network parameters [14]. Moreover, when the LCC compensation network is adopted at the secondary side, the reactive power at the secondary side could be compensated to form a unit power factor pickup [15].

One of the uniqueness of WPT systems is the high spatial freedom of the coils. This means the air-gap variation and misalignment of the transmitting and receiving coils are inevitable. Usually, the system parameters and resonant frequency of the primary and secondary resonant tanks change when the coupling condition changes [16]. With traditional compensation topologies, to achieve high efficiency, a tuning method is needed to maintain the resonance when the air gap changes or misalignment happens. There are two main methods, namely, frequency control [17], [18] and impedance matching [19], [20]. In [18], the frequency characteristics of the WPT system is studied, and a method to automatically tune the operating frequency to maintain optimum efficiency is proposed. Phase-locked loop techniques are able to tune the operating frequency to track the resonant frequency that will change due to the variation of gap length, misalignment, and tolerance variation of the tuning components [17]. Impedance

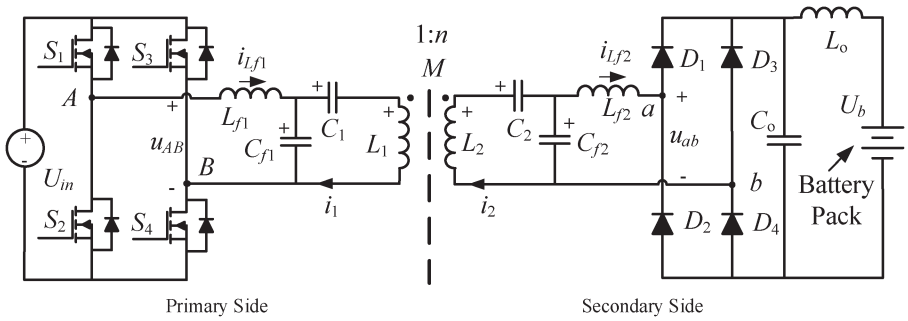

Fig. 1. Double-sided LCC compensation topology for WPT.

matching is adopted in [20]. A tuning circuit was added in the SS structure to increase the efficiency by changing the resonant frequency to match the operating frequency. Similarly, an automated impedance matching system was designed in [19], and in [21], two ways for tuning the primary tank are introduced: the primary capacitance and inductance. For the SS structure, when the capacitor is tuned with the coil self-inductance, a fully resonant characteristic can be realized [10], [22]. In this case, the resonant frequency is independent with the load and coupling condition. However, for SS compensation, the primary coil current varies with the coupling coefficient and load condition. There are a few benefits to have a constant primary coil current. When a coil is designed, the rated current of the coil is determined. A constant current feature can make the coil work at its rated condition easily. For a track form coil at the primary side in dynamic roadway charging, multiple receiving coils could be powered, which also prefers a constant current in the track. Moreover, the power is related to the primary-coil current, coupling, and load condition. When the coil current is not a function of coupling and load, the control of power can be simplified. To keep a constant primary-coil current, additional phase shift or duty cycle control is usually adopted to regulate the coil current, which increases the control complexity, circulating energy in the inverter, and the risk of losing soft switching condition.

The compensation network and the corresponding control method are the most important and difficult aspects in the design of a wireless charging system. In this paper, the compensation network design is focused. A double-sided LCC compensation topology and its parameter design are proposed. The topology consists of one inductor and two capacitors at both the primary and secondary sides. With the proposed method, the resonant frequency of the compensated coils is independent of the coupling coefficient and the load condition. The WPT system can work at a constant frequency, which eases the control and narrows the occupation of frequency bandwidth. Nearly unit power factors can be achieved for both the primary-side and secondary-side converters in the whole range of coupling and load conditions; thus, high efficiency for the overall WPT system is easily achieved. A parameter tuning method is also proposed and analyzed to achieve ZVS operation for the MOSFET-based inverter. The proposed method is more attractive in an environment where the coupling coefficient keeps changing, such as the electric vehicle charging application. Moreover, due to its symmetrical structure, the proposed method can be used in a bidirectional WPT system. Simulation and experimental results verified analysis and validity of the proposed compensation network and the tuning method. A prototype with output power of 7.7 kW for electric vehicles was built, and 96% efficiency from dc power source to battery load was achieved.

The double-sided LCC compensation network, as well as a theoretical analysis, is presented in Section II. The tuning method for realizing ZVS is discussed in Section III. The design method for the proposed topology is introduced in Section IV. Experimental, simulation, and theoretical results are compared in Section V. The conclusions are summarized in Section VI.

II. Proposed Topology and Analysis

The proposed double-sided LCC compensation network and corresponding power electronics circuit components are shown in Fig. 1. $S_1 \sim S_4$ are four power MOSFETs in the primary side. $D_1 \sim D_4$ are the secondary-side rectifier diodes. L_1 and L_2 are the self-inductances of the transmitting and receiving coils, respectively. L_{f1} and C_{f1} and C_1 are the primary-side compensation inductor and capacitors, respectively. L_{f2} and C_{f2} and C_2 are the secondary-side compensation components, respectively. M is the mutual inductance between the two coils. Here, u_{AB} is the input voltage applied on the compensated coil, and u_{ab} is the output voltage before the rectifier diodes. i_1, i_2, i_{Lf1}, and i_{Lf2} are the currents on L_1, L_2, L_{f1}, and L_{f2}, respectively. In the following analysis, $\mathbf{U}_{AB}$, $\mathbf{U}_{ab}$, $\mathbf{I}_1$, $\mathbf{I}_2$, $\mathbf{I}_{Lf1}$, and $\mathbf{I}_{Lf2}$ are adopted to represent the phasor form of the corresponding variables.

For the first step, a concise characteristic of the proposed compensation network will be given by analyzing the first-order harmonics of the square voltage waveform at the switching frequency. The resistance on all the inductors and capacitors are neglected for simplicity of analysis. The accuracy of the approximations will be verified by circuit simulation and experiments in the latter sections. The equivalent circuit of the circuit in Fig. 1 referred to the primary side is derived as shown in Fig. 2. The apostrophe symbols indicate the variables of the secondary side referred to the primary side. We define the turns ratio of the secondary to primary side as

$$n = \sqrt{\frac{L_2}{L_1}}. \tag{1}$$

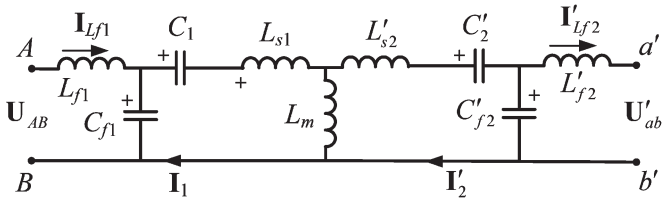

Fig. 2. Equivalent circuit referred to the primary side of the proposed topology.

The variables in Fig. 2 can be expressed by the following:

$$\begin{aligned} L_m &= k \cdot L_1 \\ L_{s1} &= (1-k) \cdot L_1 \\ L'_{s2} &= (1-k) \cdot L_2/n^2 \\ L'_{f2} &= \frac{L_{f2}}{n^2} \\ C'_2 &= n^2 \cdot C_2 \\ C'_{f2} &= n^2 \cdot C_{f2} \\ U'_{ab} &= \frac{U_{ab}}{n} \end{aligned} \tag{2}$$

where L_m is the magnetizing inductance referred to the primary side. The apostrophe symbols, which also appear in the equations after, mean the converted values that refer to the primary side.

For a high-order system in Fig. 1, there are multiple resonant frequencies. In this paper, we do not focus on the overall frequency-domain characteristics. Only one frequency point, which could be tuned to a constant resonant frequency, is studied. Here, the resonant means the input voltage $\mathbf{U}_{AB}$ and current $\mathbf{I}_{Lf1}$ of the compensated coil system are in phase. The circuit parameters are designed by the following equations to achieve a constant resonant frequency for the topology:

$$\begin{aligned} L_{f1} \cdot C_{f1} &= \frac{1}{\omega_0^2} \\ L_{f2} \cdot C_{f2} &= \frac{1}{\omega_0^2} \\ L_1 - L_{f1} &= \frac{1}{\omega_0^2 C_1} \\ L_2 - L_{f2} &= \frac{1}{\omega_0^2 C_2} \end{aligned} \tag{3}$$

where ω_0 is the angular constant resonant frequency, which is only relevant to inductors and capacitors in the system, independent of coupling coefficient k and load conditions.

Under the above rules, the circuit characteristics will be analyzed at resonant frequency ω_0. According to superposition theory, the effect of $\mathbf{U}_{AB}$ and $\mathbf{U}'_{ab}$ can be analyzed separately, as shown in Fig. 3. The dashed line means there is no current on that path. Fig. 3(a) is used to analyze the effect of $\mathbf{U}_{AB}$. The additional subscript AB indicates that current is contributed by $\mathbf{U}_{AB}$. To make the analysis clear, the series-connected capacitor and inductor branches, i.e., C_1 and L_{s1} and C'_2 and L'_{s2}, are expressed using equivalent inductances L_{e1} and L'_{e2}, where

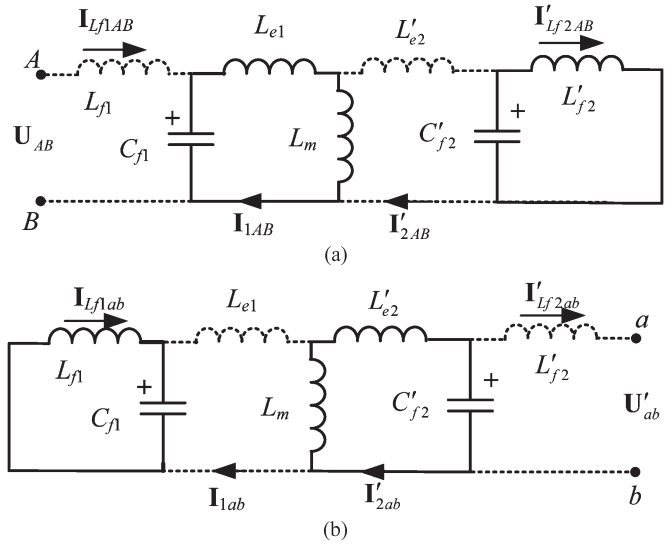

Fig. 3. Circuit status at resonant frequency. (a) When only $\mathbf{U}_{AB}$ is applied. (b) When only $\mathbf{U}'_{ab}$ applied.

$$L_{e1} = \frac{1}{j\omega_0} \cdot \left(\frac{1}{j\omega_0 C_1} + j\omega_0 L_{s1} \right) = L_{f1} - k \cdot L_1 \tag{4}$$

$$L'_{e2} = \frac{1}{j\omega_0} \cdot \left(\frac{1}{j\omega_0 C'_2} + j\omega_0 L'_{s2} \right) = L'_{f2} - k \cdot L_1. \tag{5}$$

L'_{f2} and C'_{f2} form a parallel resonant circuit, which can be regarded as an open circuit at the resonant frequency ω_0. Thus, $\mathbf{I}'_{2AB} = 0$. In the left part of the circuit, L_{e1} and L_m are connected in series, and

$$L_{e1} + L_m = L_{f1} - k \cdot L_1 + k \cdot L_1 = L_{f1}. \tag{6}$$

It forms another parallel resonant circuit with C_{f1} at the same resonant frequency ω_0. Thus, $\mathbf{I}_{Lf1AB} = 0$. Because there is no current through L_{f1} and L'_{e2}, the voltage on C_{f1} equals $\mathbf{U}_{AB}$, and the voltage on C_{f2} equals the voltage on L_m. $\mathbf{I}_{1AB}$ and $\mathbf{I}'_{Lf2AB}$ can be easily solved, i.e.,

$$\mathbf{I}_{1AB} = \frac{\mathbf{U}_{AB}}{j\omega_0 L_{f1}} \tag{7}$$

$$\mathbf{I}'_{Lf2AB} = \frac{k\mathbf{U}_{AB} L_1}{j\omega_0 L_{f1} L'_{f2}}. \tag{8}$$

When $\mathbf{U}'_{ab}$ is applied, the analysis is similar to that when $\mathbf{U}_{AB}$ is applied. An additional subscript $_{ab}$ is added to indicate that the current is contributed by $\mathbf{U}_{ab}$.

The solutions are $\mathbf{I}'_{Lf2ab} = 0$, $\mathbf{I}_{1ab} = 0$, and

$$\mathbf{I}'_{2ab} = -\frac{\mathbf{U}'_{ab}}{j\omega_0 L'_{f2}} \tag{9}$$

$$\mathbf{I}_{Lf1ab} = -\frac{k\mathbf{U}'_{ab} L_1}{j\omega_0 L_{f1} L'_{f2}}. \tag{10}$$

$\mathbf{U}'_{ab}$ is a passive voltage generated according to the conduction mode of diodes $D_1 \sim D_4$. It should be in phase with $\mathbf{I}'_{Lf2}$. Since $\mathbf{I}'_{Lf2ab} = 0$, $\mathbf{U}'_{ab}$ is in phase with $\mathbf{I}'_{Lf2AB}$. If we take $\mathbf{U}_{AB}$ as the reference, $\mathbf{U}_{AB}$ and $\mathbf{U}'_{ab}$ can be expressed as

$$\mathbf{U}_{AB} = U_{AB}\angle 0^\circ \tag{11}$$

$$\mathbf{U}'_{ab} = \frac{U'_{ab}}{j} = U'_{ab}\angle\varphi = U'_{ab}\angle -90^\circ \tag{12}$$

where φ is the phase by which $\mathbf{U}_{ab}$ leads $\mathbf{U}_{AB}$. From (11) and (12), we can see $\mathbf{U}'_{ab}$ lags $\mathbf{U}_{AB}$ by 90°. We substitute (2), (11) and (12) into (7)–(10) and sum up the current generated by $\mathbf{U}_{AB}$ and $\mathbf{U}'_{ab}$ to get

$$\mathbf{I}_{Lf1} = \mathbf{I}_{Lf1ab} = \frac{kL_1U'_{ab}}{\omega_0 L_{f1}L'_{f2}}\angle 0^\circ = \frac{k\sqrt{L_1L_2}U_{ab}}{\omega_0 L_{f1}L_{f2}}\angle 0^\circ \tag{13}$$

$$\mathbf{I}_1 = \mathbf{I}_{1AB} = \frac{U_{AB}}{j\omega_0 L_{f1}} = \frac{U_{AB}}{\omega_0 L_{f1}}\angle -90^\circ \tag{14}$$

$$\mathbf{I}_2 = \frac{\mathbf{I}'_2}{n} = \frac{\mathbf{I}'_{2ab}}{n} = \frac{U'_{ab}}{n\cdot\omega_0 L'_{f2}}\angle 0^\circ = \frac{U_{ab}}{\omega_0 L_{f2}}\angle 0^\circ \tag{15}$$

$$\mathbf{I}_{Lf2} = \frac{\mathbf{I}'_{Lf2}}{n} = \frac{\mathbf{I}'_{Lf2AB}}{n} = \frac{k\sqrt{L_1L_2}\cdot U_{AB}}{\omega_0 L_{f1}L_{f2}}\angle -90^\circ. \tag{16}$$

From (11) and (13), we can see that the input voltage and current are in phase. The unit power factor for the converter is achieved. From (12) and (16), we can see that the output voltage and current are in phase. The unit power factor for the output rectifier is also achieved. Moreover, the phase relation does not rely on the coupling coefficient and battery voltage. Thus, resonant condition could be achieved, regardless of the coupling and load condition. The transferred power can be calculated by

$$P = \mathbf{U}_{AB}\cdot\mathbf{I}_{Lf1} = \frac{\sqrt{L_1L_2}}{\omega_0 L_{f1}L_{f2}}\cdot kU_{AB}U_{ab}. \tag{17}$$

It can be seen that the output power is proportional to the coupling coefficient k, input voltage U_{AB}, and output voltage U_{ab}. Thus, a buck or boost converter can be inserted into either before the primary-side inverter or after the secondary-side rectifier to control the output power. For some applications, such as opportunity charging or dynamic charging for electric vehicles, an accurate continuous power is not necessary. In this case, the charging power can be controlled by switching the system between the maximum and zero output power. Thus, the buck or boost converter can be omitted.

III. Parameter Tuning for Zero Voltage Switching

If the coils and compensation network parameters are designed exactly according to the above rules, all the MOSFETs will be turned on and off at a ZCS condition. However, ZCS is not a perfect soft switching condition in converters containing MOSFETs and diodes. To minimize the switching loss, it is better that all switches are turned on and off at a zero voltage switching (ZVS) condition. The parasitic output capacitance of the MOSFET holds the voltage close to zero during the turn-off transition. Therefore, the turn-off switching loss is very small [23]. However, in the turn-on transition, ZVS operation is required to prevent both body diode reverse recovery and parasitic output capacitance from inducing switching loss. To realize ZVS for a MOSFET, the body diode should conduct before the MOSFET does. It is essential that the MOSFET needs to be turned on at a negative current. For a full-bridge converter, this means the input impedance of the resonant network should be inductive. In this case, the resonant current lags the resonant voltage that forms the ZVS operation condition for all MOSFETs.

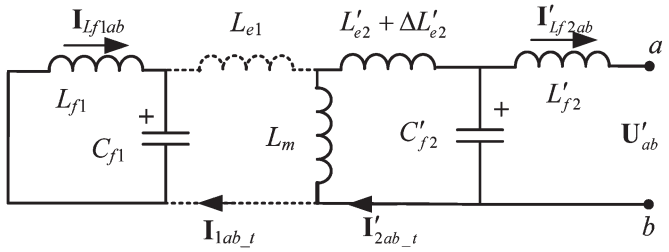

Fig. 4. Equivalent circuit referred to the primary side.

In this paper, the ZVS operation condition refers to ensuring the turn-off current to be positive to realize ZVS turn on of another MOSFET in the same arm. There can be several ways to tune the system parameters to ensure that the MOSFETs turn off at a positive current. Here, one simple way is introduced and analyzed.

To achieve ZVS, we just slightly increase the value of L_{e2}. As shown in Fig. 4, the change of L_{e2} is $\Delta L'_{e2}$. Moreover, the superposition method is used to analyze the tuned circuit. When $\mathbf{U}_{AB}$ is applied to the circuit, the equivalent circuit is the same as in Fig. 3(a), i.e., $\mathbf{I}_{Lf1AB}$ is zero. However, when $\mathbf{U}'_{ab}$ is applied, $\mathbf{I}'_{Lf2ab}$ is not zero. We solve the circuit again with the variation of $\Delta L'_{e2}$, and the following equations can be derived:

$$\mathbf{I}'_{Lf2ab\_1st} = -j\cdot\frac{\mathbf{U}'_{ab}}{\omega_0\cdot L'_{f2}}\cdot\frac{\Delta L'_{e2}}{L'_{f2}} \tag{18}$$

$$\begin{aligned}\mathbf{I}'_{Lf2\_1st} &= \mathbf{I}'_{Lf2AB} + \mathbf{I}'_{Lf2ab\_1st}\\ &= \frac{kU_{AB}L_1}{j\omega_0 L_{f1}L'_{f2}} - j\\ &\quad\cdot\frac{U'_{ab}\cdot(\cos\varphi + j\cdot\sin\varphi)}{\omega_0\cdot L'_{f2}}\cdot\frac{\Delta L'_{e2}}{L'_{f2}}\\ &= \frac{U'_{ab}\cdot\sin\varphi\cdot\Delta L'_{e2}}{\omega_0\left(L'_{f2}\right)^2} - j\\ &\quad\cdot\left(\frac{U'_{ab}\cdot\cos\varphi\cdot\Delta L'_{e2}}{\omega_0\left(L'_{f2}\right)^2} + \frac{kU_{AB}L_1}{\omega_0 L_{f1}L'_{f2}}\right)\end{aligned} \tag{19}$$

$$\begin{aligned}\mathbf{I}_{Lf2\_1st} &= \frac{\mathbf{I}'_{Lf2\_1st}}{n}\\ &= \frac{U_{ab}\cdot\sin\varphi\cdot\Delta L_{e2}}{\omega_0 L_{f2}^2} - j\cdot\frac{kU_{AB}\sqrt{L_1L_2}}{\omega_0 L_{f1}L_{f2}} - j\\ &\quad\cdot\frac{U_{ab}\cdot\cos\varphi\cdot\Delta L_{e2}}{\omega_0 L_{f2}^2}.\end{aligned} \tag{20}$$

In the given equations, the subscript 1st is used to indicate that it is the first harmonic component of the corresponding item.

The phase of $\mathbf{U}_{ab}$ is φ. Equation (12) shows that φ is -90° when ΔL_{e2} is zero. When we increase L_{e2} to realize ZVS, the change of L_{e2} is relatively small; therefore, φ is still close to -90°. We have $\sin\varphi \approx -1$, $\cos\varphi \approx 0$, and $\Delta L_{e2} < L_{f2}$. Usually, the additional inductors L_{f1} and L_{f2}, which are used as a reactive power compensator, are designed such that they are much smaller than the main coils. The following approximation can be obtained from (20):

$$\cos\varphi_1 \approx -\cot\varphi_1 \approx -\frac{U_{ab}}{U_{AB}} \cdot \frac{\Delta L_{e2} \cdot L_{f1}}{L_{f2} \cdot k\sqrt{L_1 L_2}} \tag{21}$$

where φ_1 $(-90^\circ < \varphi_1 \ll -180^\circ)$ is the phase by which $\mathbf{I}_{Lf2\_1st}$ leads $\mathbf{U}_{AB}$.

To reduce the switching loss, we prefer to achieve ZVS condition at a minimum turn-off current. This means that, at the switching point, the current is close to zero. The current slew rate at the switching point is high. A small phase error in the analysis will bring relatively large current error. If the phase error falls into the inductive region, it means a higher turn-off current and higher switching loss. If the phase error falls into the capacitive region, the turn-off current may be negative. It means ZVS is lost, and severe reverse recovery in the MOSFET diode will occur. This will bring high switching loss and electromagnetic interference (EMI) problem. Therefore, the analysis accuracy of the turn-off current is very important. The high-order harmonics of the square voltage should be considered. The inductor–capacitor network from the primary side to the secondary side is a high-order filter. For the high-order harmonics, the interaction between the primary and secondary sides can be neglected. Thus, the high-order current on L_{f2} can be roughly calculated by

$$\begin{aligned}
\mathbf{I}_{Lf2_3rd} &\approx -\frac{\mathbf{U}_{ab_3rd}}{j\cdot 3\omega_0 L_{f2} + \frac{1}{j\cdot 3\omega_0 C_{f2}}} = j\frac{3\mathbf{U}_{ab_3rd}}{8\omega_0 L_{f2}} \\
\mathbf{I}_{Lf2_5th} &\approx -\frac{\mathbf{U}_{ab_5th}}{j\cdot 5\omega_0 L_{f2} + \frac{1}{j\cdot 5\omega_0 C_{f2}}} = j\frac{5\mathbf{U}_{ab_5th}}{24\omega_0 L_{f2}} \\
&\cdots \\
\mathbf{I}_{Lf2_(2k+1)th} &\approx -\frac{\mathbf{U}_{ab_(2k+1)th}}{j\cdot (2k+1)\omega_0 L_{f2} + \frac{1}{j\cdot (2k+1)\omega_0 C_{f2}}} \\
&= j\frac{(2k+1)\mathbf{U}_{ab_(2k+1)th}}{((2k+1)^2-1)\,\omega_0 L_{f2}} \\
&\cdots .
\end{aligned} \tag{22}$$

According to (22), the phase difference between $\mathbf{U}_{ab\_mth}$ and $\mathbf{I}_{Lf2\_mth}$ is 90°. Therefore, when $\mathbf{U}_{ab}$ jumps at the time that $i_{Lf2} = 0$, i_{Lf2_mth} reaches the peak. Moreover, the peak value can be calculated by

$$\begin{aligned}
\max\left\{\sum i_{Lf2_mth}\right\} &= \sqrt{2}\cdot\sum_{k=1}^{\infty} I_{Lf2_(2k+1)th} \\
&= \sqrt{2}\cdot\sum_{k=1}^{\infty}\frac{1}{((2k+1)^2-1)}\frac{U_{ab}}{\omega_0 L_{f2}} \\
&= \frac{\sqrt{2}}{4}\cdot\frac{U_{ab}}{\omega_0 L_{f2}}.
\end{aligned} \tag{23}$$

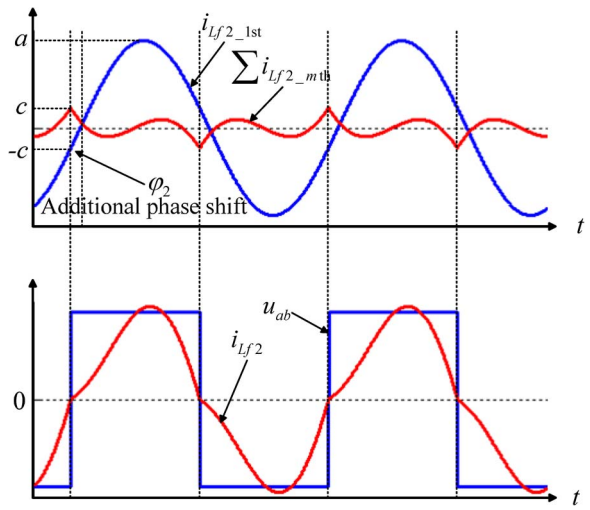

Fig. 5. Effect of all high-order currents. $a = \sqrt{2}\cdot(k\sqrt{L_1L_2}U_{AB}/\omega_0 L_{f1}L_{f2})$, and $c = \sqrt{2}\cdot(U_{ab}/4\omega_0 L_{f2})$.

The phase φ_2, by which $\mathbf{U}_{ab}$ leads $\mathbf{I}_{Lf2\_1st}$, is close to 0 $(0 < \varphi_2 \ll 90^\circ)$ and can be easily obtained by

$$\sin\varphi_2 = \frac{\sqrt{2}\cdot\sum_{k=1}^{\infty} I_{Lf2\_(2k+1)th}}{\sqrt{2}\cdot I_{Lf2\_1st}} \approx \frac{1}{4}\cdot\frac{U_{ab}}{U_{AB}}\cdot\frac{L_{f1}}{k\sqrt{L_1L_2}}. \tag{24}$$

Fig. 5 shows the effect of the high-order harmonic currents. The sign of u_{ab} is determined by i_{Lf2}, which is a composition of both the first- and high-order harmonic currents.

From (21) and (24), the following equation can be derived:

$$\begin{aligned}
\cos\varphi &= \cos(\varphi_1+\varphi_2) = \cos\varphi_1\cos\varphi_2 - \sin\varphi_1\sin\varphi_2 \\
&\approx \cos\varphi_1 + \sin\varphi_2 \\
&\approx -\frac{U_{ab}}{U_{AB}}\cdot\frac{L_{f1}}{k\sqrt{L_1L_2}}\cdot\left(\frac{\Delta L_{e2}}{L_{f2}} - \frac{1}{4}\right), \\
\mathbf{I}_{Lf1_1st} &= -\frac{k\mathbf{U}'_{ab}L_1}{j\omega_0 L_{f1}L'_{f2}} = -\frac{kU'_{ab}(\cos\varphi + j\cdot\sin\varphi)L_1}{j\omega_0 L_{f1}L'_{f2}} \\
&= -\frac{kU'_{ab}\sin\varphi L_1}{\omega_0 L_{f1}L'_{f2}} - \frac{kU'_{ab}\cos\varphi L_1}{j\cdot\omega_0 L_{f1}L'_{f2}} \\
&\approx \frac{kU'_{ab}L_1}{\omega_0 L_{f1}L'_{f2}} + \frac{\frac{U_{ab}^2}{U_{AB}}\left(\frac{\Delta L_{e2}}{L_{f2}} - \frac{1}{4}\right)}{j\cdot\omega_0 L_{f2}} \\
&= \frac{kU_{ab}\sqrt{L_1L_2}}{\omega_0 L_{f1}L_{f2}} + \frac{\frac{U_{ab}^2}{U_{AB}}\left(\frac{\Delta L_{e2}}{L_{f2}} - \frac{1}{4}\right)}{j\cdot\omega_0 L_{f2}}.
\end{aligned} \tag{25, 26}$$

From (26), we can see an additional reactive current item is introduced. This current will increase the MOSFET turn-off current to achieve ZVS. For the primary side, similar to the analysis of the secondary side for the high-order harmonics effect, the following equations can be obtained:

$$\begin{aligned}
\max\left\{\sum i_{Lf1_mth}\right\} &= \sqrt{2}\cdot\sum_{k=1}^{\infty} I_{Lf1_(2k+1)th} \\
&= \sqrt{2}\cdot\sum_{k=1}^{\infty}\frac{1}{((2k+1)^2-1)}\frac{U_{AB}}{\omega_0 L_{f1}} \\
&= \frac{\sqrt{2}}{4}\cdot\frac{U_{AB}}{\omega_0 L_{f1}}.
\end{aligned} \tag{27}$$

The MOSFET turn-off current is a composition of both the first-order and high-order harmonic currents. From (26) and (27), the MOSFET turn-off current can be calculated as

$$I_{\mathrm{OFF}} = \sqrt{2}\left(\frac{\frac{U_{ab}^2}{U_{AB}}\left(\frac{\Delta L_{e2}}{L_{f2}} - \frac{1}{4}\right)}{\omega_0 L_{f2}} + \frac{U_{AB}}{4\omega_0 L_{f1}}\right). \tag{28}$$

According to the MOSFET parameters, a minimum turn-off current to achieve ZVS can be determined [24]. Then, a suitable ΔL_{e2} can be designed to ensure that there is enough turn-off current to achieve ZVS for the whole operation range. To ensure I_{OFF} is greater than a certain positive value, the following equation should be satisfied:

$$\frac{\Delta L_{e2}}{L_{f2}} \geq \frac{1}{4}. \tag{29}$$

According to (28) and (29), the lower the output voltage is, the smaller the turn-off current is. The minimal turn-off current can be derived as

$$I_{\mathrm{OFF\_min}} = \frac{\sqrt{2}\cdot U_{ab\_\min}}{\omega_0 \cdot L_{f2}}\sqrt{\frac{\Delta L_{e2}}{L_{f1}} - \frac{1}{4}\frac{L_{f2}}{L_{f1}}} \tag{30}$$

where $U_{ab\_\min}$ is the minimum rms value of the output voltage before rectifier.

The minimum turn-off current is reached when

$$U_{AB} = U_{ab\_\min}\cdot\sqrt{4\cdot\left(\frac{\Delta L_{e2}}{L_{f2}} - \frac{1}{4}\right)\cdot\frac{L_{f1}}{L_{f2}}}. \tag{31}$$

Once the minimum MOSFET turn-off current is obtained, ΔL_{e2} can be calculated by

$$\Delta L_{e2} = \frac{1}{4}L_{f2} + \frac{I_{\mathrm{OFF\_min}}^2\cdot\omega_0^2\cdot L_{f1}\cdot L_{f2}^2}{U_{ab\_\min}^2}. \tag{32}$$

When the parameters are tuned for ZVS, the change of active power transferred is very limited. The conclusion could be obtained by analyzing the change of $\mathbf{I}_{Lf2\_1\mathrm{st}}$ and the phase between output current and voltage. In (20), the first term has one relative small item, and its contribution to the amplitude is negligible. The last term is a product of two relative small items, which can also be neglected. Compared with (13), the amplitude of $\mathbf{I}_{Lf2\_1\mathrm{st}}$ is almost the same. From (24), we can see the phase between the output current and voltage has no relation with ΔL_{e2}. Thus, ΔL_{e2} does not have an obvious impact on the active power transferred. However, if the harmonics are considered, the output power in (17) should be revised to

$$P = \frac{\sqrt{L_1 L_2}}{\omega_0 L_{f1} L_{f2}}\cdot kU_{AB}U_{ab}\cos\varphi_2 \tag{33}$$

where $\cos\varphi_2$ can be calculated from (24). If U_{AB} is not too low, $\cos\varphi_2$ will be close to 1. The output power could be calculated by both (17) and (33).

The decomposition of current harmonics adopted in this section is a refinement of a similar approach that was used in the analysis of a ZCS LCC-compensated resonant converter [14]. In the referenced paper, the battery load was considered an equivalent impedance, which is a kind of first harmonics approximation. Although the high-order harmonics is hardly transferred between the primary-side and secondary-side coils, it does affect the reactive power at the secondary side, which will change the primary-side turn-off current. Here, the current harmonics are considered at both the primary and secondary sides. The secondary-side phase difference between the voltage and current fundamental harmonic could be solved, which means that the reactive power of the battery load with a rectifier was solved. In this way, (28) gives a direct method to calculate the turn-off current by the input and output voltages instead of an equivalent impedance of the battery load, which could be used to optimize the parameters easily.

TABLE I
WIRELESS BATTERY CHARGER SPECIFICATIONS

Spec / Parameter	Value
Input DC voltage	< 425 V
Output battery voltage	300V~450V
Nominal gap	200 mm
Coupling coefficient[1]	0.18~0.32
Transmitting coil inductance[2]	350~370 μH
Transmitting coil AC resistance	~500 mΩ
Receiving coil inductance[2]	350~370 μH
Receiving coil AC resistance	~500 mΩ
Switching frequency	79 kHz
Maximum power[3]	~8 kW
Maximum efficiency[3]	~97.1%

[1]The coupling coefficient varies because of misalignment. Its value is related to the coil design, which is not the focus of this paper.
[2]The main coil inductance changes a little bit when the position of the two coils changes. A middle value 360 μH was selected in the design stage.
[3]The rated output power is designed as 8kW with the maximum efficiency of 97.1%. Due to the parameter variations, the maximum efficiency of 96% was reached at 7.7kW.

TABLE II
COMPENSATION NETWORK PARAMETERS

Parameter	Design value
L_{f1}	67μH
L_{f2}	67μH
C_{f1}	60.6nF
C_{f2}	60.6nF
C_1	14nF
C_2	15.1nF

IV. PARAMETERS DESIGN

In this section, an 8-kW WPT system is designed according to the above principle. A comparison between the simulation results and the analytical results will be given in the following section to verify the effectiveness of the above analysis.

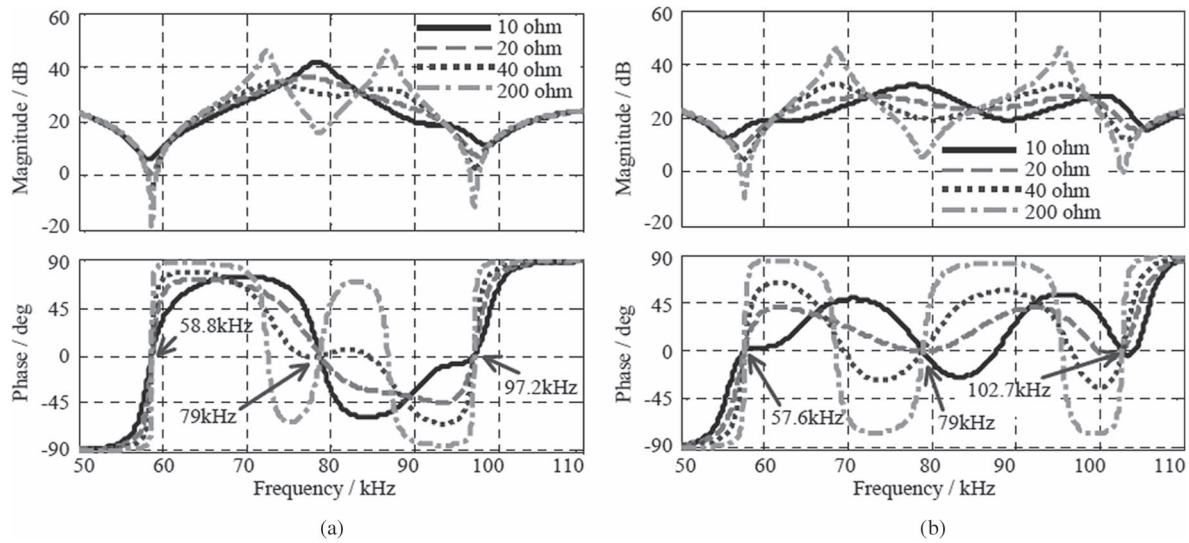

Fig. 6. Frequency characteristics of the input impedance. (a) $k = 0.18$. (b) $k = 0.32$.

The specifications of the wireless battery charger are listed in Table I. Since the ratio between the input voltage and the output voltage is around 1, the transmitting and receiving coils are designed to have to same size. Thus, from (3), we should design $L_{f1} = L_{f2}$. From Table I and (17), we can get

$$L_{f1} = L_{f2} = \sqrt{\frac{k_{\max} U_{AB} U_{ab}}{\omega_0 P_{\max}} \cdot L_1}$$

$$= \sqrt{\frac{0.32 \times \frac{2\sqrt{2}}{\pi} \times 425 \times \frac{2\sqrt{2}}{\pi} \times 450}{2\pi \times 79 \times 10^3 \times 8 \times 10^3} \cdot 360 \times 10^{-6}}\ \text{H}$$

$$\approx 67\ \mu\text{H}. \tag{34}$$

The value of C_{f1} and C_{f2} can be calculated from (3) as follows:

$$C_{f1} = C_{f2} = \frac{1}{\omega_0^2 L_{f1}} \approx 60.6\ \text{nF}. \tag{35}$$

C_1 and C_2 can also be calculated from (3) as follows:

$$C_1 = C_2 = \frac{1}{\omega_0^2 (L_1 - L_{f1})} \approx 14\ \text{nF}. \tag{36}$$

Then, a variation of ΔL_{e2} should be designed to increase the turn-off current for MOSFETs to achieve ZVS. Once the minimum turn-off current for ZVS is obtained, ΔL_{e2} can be designed using (32). For different MOSFETs and dead-time settings, the minimum turn-off current is different. For a 8-kW system, usually, a MOSFET with 80-A continuous conduction capability can be adopted. Fairchild FCH041N60E N-Channel MOSFET was chosen as the main switches. The switches are rated at 600 V and 48 (75°C)–77 A (25°C). According to the parameters of the MOSFET, the calculated dead time is 600 ns. To guarantee ZVS in this mode, the turn-off current must be large enough to discharge the junction capacitors within the dead-time, which can be represented as follows: [24]

$$I_{\text{OFF}} \geq \frac{4 C_{\text{oss}} U_{AB,\max}}{t_d} \tag{37}$$

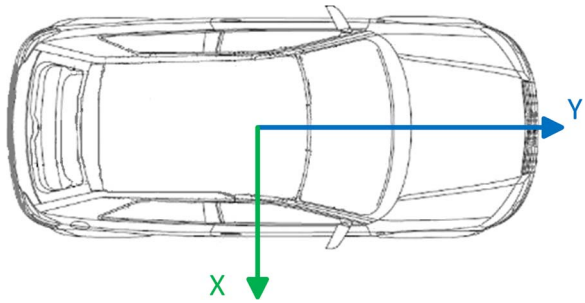

Fig. 7. Two definition of misalignments: X-misalignment is the door-to-door, or right-to-left alignment, and Y-misalignment is the front-to-rear alignment.

where $U_{AB,\max}$ is the maximum input voltage, C_{oss} is the junction capacitance, and t_d is the dead time. By using the MOSFET parameters, we can calculate the turn-off current that should be larger than 2 A to realize ZVS. Thus, we design the minimum turn-off current $I_{\text{OFF\_min}}$ to be 3 A.

By substituting (34)–(36), and $I_{\text{OFF\_min}}$ into (32), we can get

$$\Delta L_{e2} = \frac{1}{4} L_{f2} + \frac{I_{\text{OFF\_min}}^2 \cdot \omega_0^2 \cdot L_{f1} \cdot L_{f2}^2}{2 \cdot U_{ab\_\min}^2}$$

$$= \left(\frac{67}{4} + \frac{3^2 \cdot (2\pi \cdot 79 \times 10^3)^2 \cdot (67 \times 10^{-6})^2 \cdot 67}{2 \cdot \left(\frac{2\sqrt{2}}{\pi} \cdot 300 \right)^2} \right) \mu\text{H}$$

$$\approx 21\ \mu\text{H}. \tag{38}$$

The equivalent inductance L_{e2} is determined by C_2 and leakage inductance L_{s2}. Because of L_{s2} is related to the self-inductance and coupling, it is more complicated if we tune L_{s2} to change the value of L_{e1}. It is easier to tune C_2 to change the value of L_{e2}. From (3), we know that

$$\Delta L_{e2} = \frac{1}{\omega_0^2 C_2} - \frac{1}{\omega_0^2 (C_2 + \Delta C_2)}. \tag{39}$$

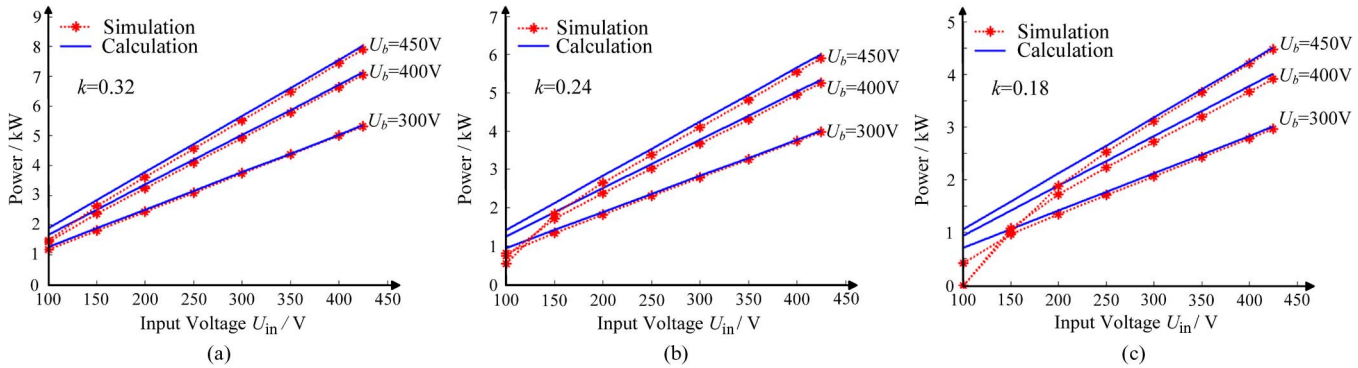

Fig. 8. Simulation and theoretical calculation results of the power levels for the designed system. (a) $k = 0.32$. (b) $k = 0.24$. (c) $k = 0.18$.

Then, the variation of C_2 can be calculated:

$$\Delta C_2 = \frac{\omega_0^2 \cdot \Delta L_{e2} \cdot C_2^2}{1 - \omega_0^2 \cdot \Delta L_{e2} \cdot C_2} \approx 1.1 \text{ nF}. \tag{40}$$

Thus, to achieve ZVS, the value of C_2 should be tuned such that it is 1.1 nF larger than the value calculated by (36). All the designed values for the compensation network are listed in Table II.

Since the system is a high-order circuit, there might be another resonant point near ω_0 with a sharp changing of the system characteristics. This may significantly affect the performance in a real system because of the parameter variations. The frequency characteristics of the circuit shown in Fig. 2 were given to check whether there is a sharp changing resonant point around ω_0. In the simulation, the value of C_2 was 14 nF to verify the analysis results in Section II. To show the load influence, a load resistor $R_{\text{ac}} = 8/\pi \cdot R_b$, where R_{b} is the equivalent resistance when the battery is charging, was connected between a' and b' in Fig. 2. When the battery charging power was between 5% to 100% power, the range of R_{ac} is roughly from 10 to 200 Ω. The frequency characteristics of the input impedance were analyzed under the coupling coefficient from 0.18 to 0.32. Two typical bode diagrams were shown in Fig. 6 with different load conditions at coupling coefficient of 0.18 and 0.32. In Fig. 6, we can see that there is a constant resonant frequency at about 79 kHz. Moreover, there are some other resonant frequencies. The lowest and highest resonant points do not change when the load changes, whereas they do change with the coupling coefficient. It should be noticed that, around ω_0, another resonant point may exist at certain conditions. However, the change from ω_0 to the neighboring resonant point is quite smooth, which means there will be no sudden change when the working frequency has a little drift from ω_0.

V. Simulation and Experiment Results

Both simulation and experiments are undertaken to verify the proposed double-sided LLC compensation network and its tuning method. The circuit parameters have been shown in Tables I and II. We define two kinds of misalignments, i.e., X-misalignment (door-to-door or right-to-left), and Y-misalignment (front-to-rear), as shown in Fig. 7. When parking a car, the X-misalignment is much harder for the driver to adjust. Therefore, we choose X-misalignments for the simulation and experiments. Various misalignments are reflected by the different coupling coefficients. In this section, three coupling coefficients, namely, $k = 0.18, 0.24, 0.32$, corresponding to X = 310, 230, and 0 mm, respectively, and three output voltages, $U_b = 300, 400,$ and 450 V, are chosen as case studies. The switching frequency is fixed at 79 kHz for all the cases.

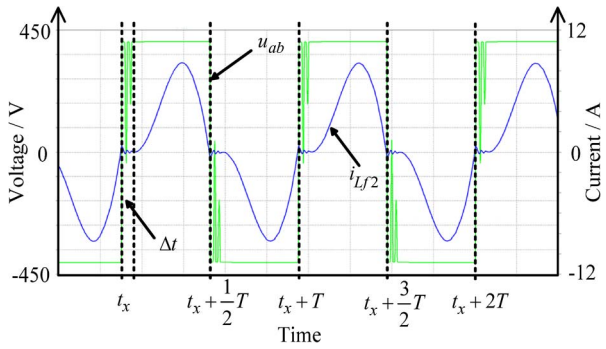

Fig. 9. Simulation waveforms of output voltage u_{ab} and current through diodes i_{Lf2} when $U_{\text{in}} = 150$ V and $U_b = 450$ V.

A. Simulation Results

A model was built in LTspice to simulate the performance of the proposed topology. The simulation results for different coupling coefficients, input voltages, and output voltages were obtained. Fig. 8 shows the comparison between simulated and calculated output power for various conditions. The output power varies linearly with the input voltages for different coupling coefficients and output voltages.

For high input voltage and high coupling coefficients, the simulation and theoretical analysis agree well with each other. However, for low input voltage and low coupling coefficients, the simulation does not agree well with the analytical results. This is because, at low input voltage and low coupling coefficient, the diodes at the secondary side do not conduct all the time between $t_x + n \cdot T/2$ and $t_x + (n+1) \cdot T/2$, which is shown in Fig. 9. A similar situation can also be found in the comparison results of turn-off current, as shown in Fig. 10.

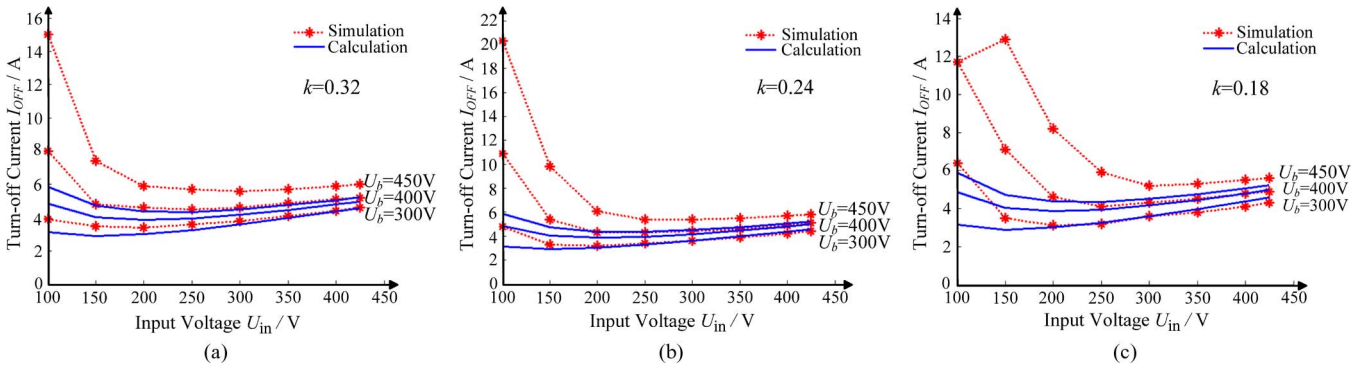

Fig. 10. Simulation and theoretical results of the MOSFETs turn-off current I_{OFF}. (a) $k = 0.32$. (b) $k = 0.24$. (c) $k = 0.18$.

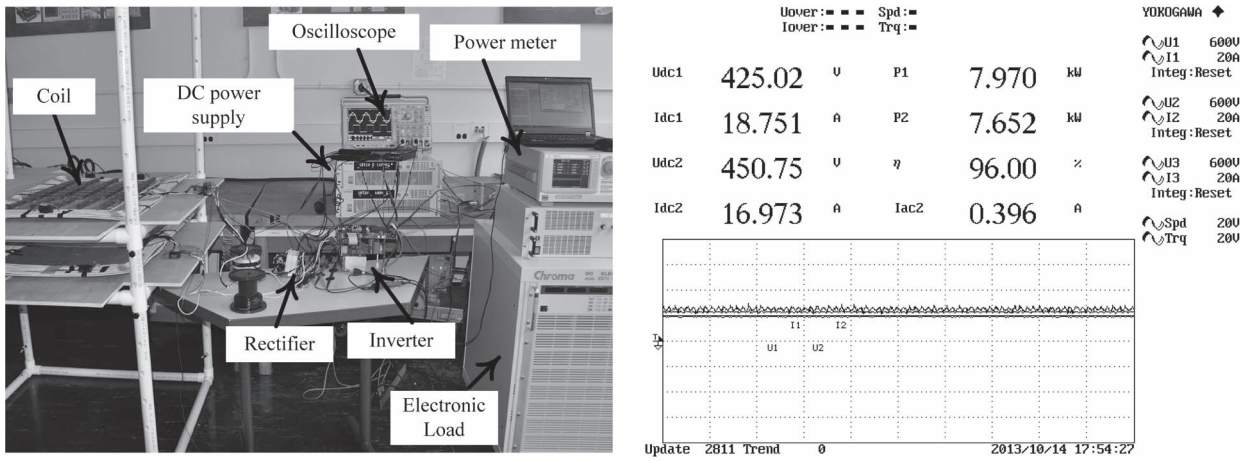

Fig. 11. Experiment setup. (a) Physical setup of the WPT system. (b) Capture of efficiency from power meter at output power of 7.7 kW.

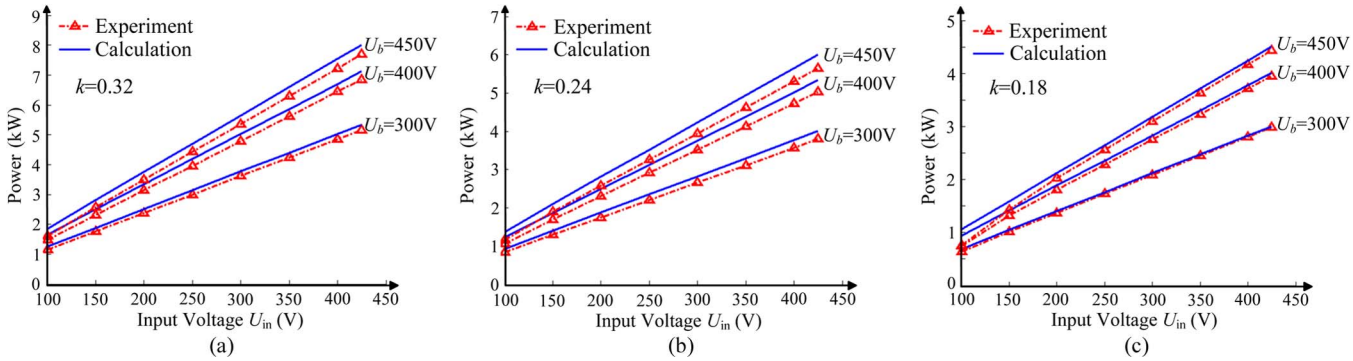

Fig. 12. Experimental and theoretical calculation results of the power levels for the wireless charger system. (a) $k = 0.32$. (b) $k = 0.24$. (c) $k = 0.18$.

B. Experimental Results

Fig. 11(a) shows the experimental setup. The coil dimension is 800 mm in length and 600 mm in width. The gap between the two coils is 200 mm. A 10-μF capacitor (C_o) and 10-μH inductor (L_o) are selected as the output filter. The coils are connected to the input inverter and output rectifier through an LCC compensation network. An electronic load at constant voltage mode was adopted to take the position of a real battery for easy voltage adjustment. Fig. 11(b) shows the efficiency screen shot from power meter Yokogawa WT1600 at output power of 7.7 kW. Udc1 and Idc1 are the input dc voltage and current, whereas Udc2 and Idc2 are the output dc voltage and current. P1 and P2 are the input and output power, and η is the efficiency from dc power supply to the electronic load. Iac2 is the output current ripple into the electronic load. Fig. 12 shows the comparison of experimental and simulation output power as a function of input voltage for three coupling coefficients and three output voltages. Different coupling coefficients are obtained by adjusting the gap and misalignment between transmitting and receiving coils. The output power matches well between simulation and experimental results, and they vary linearly with the input voltage. The same inconsistency

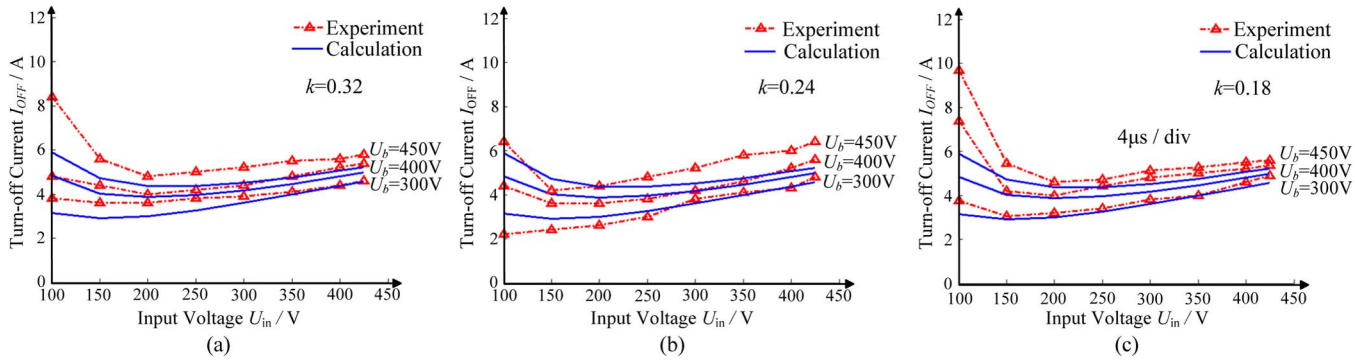

Fig. 13. Experimental and theoretical calculation results of the MOSFETs turn-off current I_{OFF}. (a) $k = 0.32$. (b) $k = 0.24$. (c) $k = 0.18$.

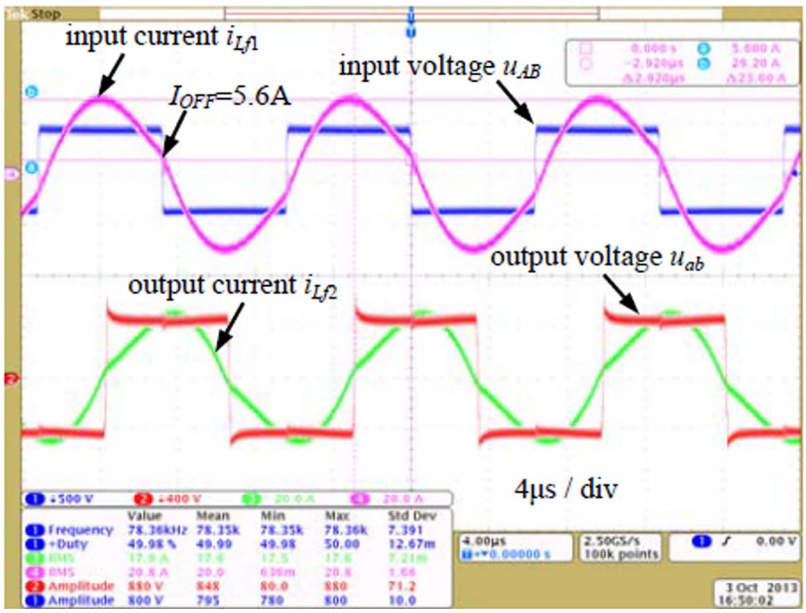

Fig. 14. Waveforms of the input voltage u_{AB} and current i_{Lf1} and output voltage u_{ab} and current i_{Lf2} when delivering power of 7.2 kW. $U_{\mathrm{in}} = 400$ V, and $U_b = 450$ V.

phenomenon happens at the low input voltage and low coupling conditions, as stated previously. The calculated and simulated maximum efficiency is 97.1%. Because of the resistance and parameter variations in the real system, the maximum efficiency of 96% was reached at output power of 7.7 kW, which is a little lower than the simulated result.

Fig. 13 shows the comparison of experimental and theoretical calculated turn-off currents of the MOSFETs. The experimental results agree well with the analytical results. Fig. 13 also verifies a good characteristic of the proposed tuning method. From (28), we can see the turn-off current is not a function of the coupling coefficient k. Once the parameters are designed and tuned, the ZVS condition could be achieved for all coupling conditions easily. The primary-side waveforms and secondary-side waveforms are shown in Fig. 14 when the system operates at steady state, delivering 7.2 kW to the load. At this operating point, input voltage $U_{\mathrm{in}} = 400$ V, output voltage $U_b = 450$ V, coupling coefficient $k = 0.32$. The results indicate a good ZVS condition with $I_{\mathrm{OFF}} = 5.6$ A. The turn-off current maintains higher than required, whereas it is quite small relative to the peak current.

Fig. 15 shows the simulation and experimental efficiencies from dc power source to the battery load for the proposed double-sided LCC compensation network for WPT system. In the experiment, we use a constant voltage mode electronic load to represent the battery pack for flexible voltage adjustment. A power meter WT1600 from Yokogawa was connected in the system to calculate the efficiency by measuring the output power from dc source and the input power to the electronic load. From Fig. 15(c), we can find that the efficiency is very high even at a large X-misalignment condition. The maximum simulated efficiency is 97.1%, whereas the maximum measured efficiency is about 96% when $U_{\mathrm{in}} = 425$ V, $U_b = 450$ V, and $k = 0.32$, as shown in Fig. 15(a). Table III gives a rough loss distribution at output power of 7.7 kW among different parts in the system. The large voltage and current dynamic range and the fast transient switching procedure make it hard to measure the loss of MOSFETs and diodes accurately. The loss of MOSFETs and diodes are estimated by spice-model-based simulation, whereas for the losses of all the other passive components, they were calculated by the current rms value and ac resistance from experiment. From Table III, we can see

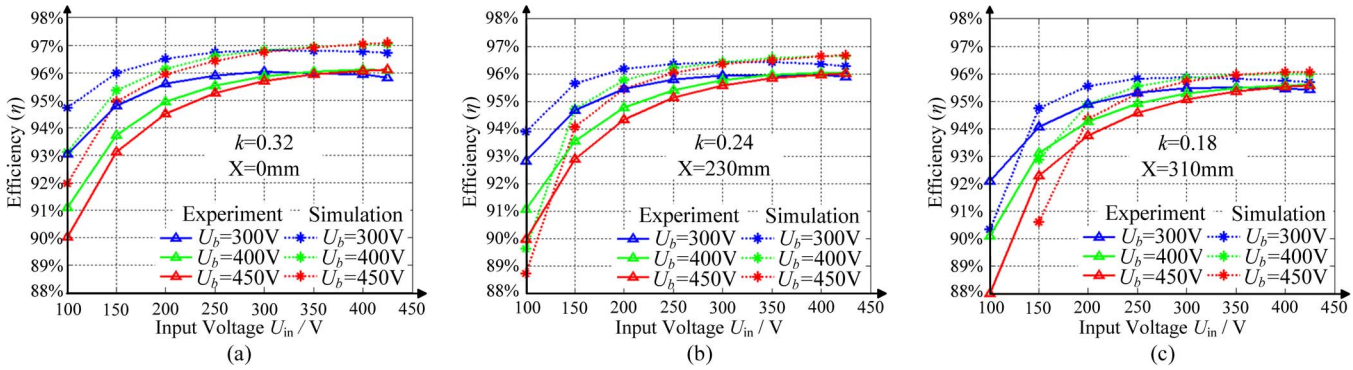

Fig. 15. Simulation and experimental efficiencies of the system when output voltages are 300, 400, and 450 V at different X-misalignments. (a) X = 0 mm. (b) X = 230 mm. (c) X = 310 mm.

TABLE III
ROUGH LOSS DISTRIBUTION AMONG THE SYSTEM

Parts	Loss ratio
Power MOSFETs	11.9 %
Main coils	52.3 %
LCC compensation network	16.7 %
Rectifier diodes	16.8 %
Output filter	2.2 %

almost half of the loss was brought by the main coils, which means if we would like to increase the efficiency further, the optimization of the coils is still the most important approach.

VI. CONCLUSION

In this paper, a double-sided LCC compensation network and its tuning method have been proposed. The novel topology and tuning method ensure that the resonant frequency is independent of coupling coefficient and load conditions, and the ZVS condition for the MOSFETs is realized. The detailed mathematical analysis of the model was presented, as well as the design method. Simulation and experimental results validated the topology and tuning method. A 7.7-kW prototype was designed and built using the method proposed in this paper. The simulated system efficiency from dc power source to battery is 97.1%, and the measured efficiency is as high as 96%.

REFERENCES

[1] A. K. A. Kurs, R. Moffatt, J. D. Joannopoulos, P. Fisher, and M. Soljacic, "Wireless power transfer via strongly coupled magnetic resonances," *Science*, vol. 317, no. 5834, pp. 83–86, Jul. 2007.

[2] A. P. Sample, D. A. Meyer, and J. R. Smith, "Analysis, experimental results, and range adaptation of magnetically coupled resonators for wireless power transfer," *IEEE Trans. Ind. Electron.*, vol. 58, no. 2, pp. 544–554, Feb. 2011.

[3] B. L. Cannon, J. F. Hoburg, D. D. Stancil, and S. C. Goldstein, "Magnetic resonant coupling as a potential means for wireless power transfer to multiple small receivers," *IEEE Trans. Power Electron.*, vol. 24, no. 7, pp. 1819–1825, Jul. 2009.

[4] A. Kurs, R. Moffatt, and M. Soljacic, "Simultaneous mid-range power transfer to multiple devices," *Appl. Phys. Lett.*, vol. 96, no. 4, pp. 044102-1–044102-3, Jan. 2010.

[5] S. Cheon *et al.*, "Circuit-model-based analysis of a wireless energy-transfer system via coupled magnetic resonances," *IEEE Trans. Ind. Electron.*, vol. 58, no. 7, pp. 2906–2914, Jul. 2011.

[6] C. K. Lee, W. X. Zhong, and S. Y. R. Hui, "Effects of magnetic coupling of nonadjacent resonators on wireless power domino-resonator systems," *IEEE Trans. Power Electron.*, vol. 27, no. 4, pp. 1905–1916, Apr. 2012.

[7] W. X. Zhong, L. C. Kwan, and S. Y. Hui, "Wireless power domino-resonator systems with noncoaxial axes and circular structures," *IEEE Trans. Power Electron.*, vol. 27, no. 11, pp. 4750–4762, Nov. 2012.

[8] T.-D. Nguyen, S. Li, W. Li, and C. C. Mi, "Feasibility study on bipolar pads for efficient wireless power chargers," in *Proc. 29th IEEE APEC Expo.*, 2014, pp. 1676–1682.

[9] A. Khaligh and S. Dusmez, "Comprehensive topological analysis of conductive and inductive charging solutions for plug-in electric vehicles," *IEEE Trans. Veh. Technol.*, vol. 61, no. 8, pp. 3475–3489, Oct. 2012.

[10] C.-S. Wang, O. H. Stielau, and G. A. Covic, "Design considerations for a contactless electric vehicle battery charger," *IEEE Trans. Ind. Electron.*, vol. 52, no. 5, pp. 1308–1314, Oct. 2005.

[11] C. Auvigne, P. Germano, D. Ladas, and Y. Perriard, "A dual-topology ICPT applied to an electric vehicle battery charger," in *Proc. 20th ICEM*, 2012, pp. 2287–2292.

[12] H. H. Wu, A. Gilchrist, K. Sealy, and D. Bronson, "A 90 percent efficient 5 kW inductive charger for EVs," in *Proc. IEEE ECCE*, 2012, pp. 275–282.

[13] U. K. Madawala and D. J. Thrimawithana, "A bidirectional inductive power interface for electric vehicles in V2G systems," *IEEE Trans. Ind. Electron.*, vol. 58, no. 10, pp. 4789–4796, Oct. 2011.

[14] Z. Pantic, B. Sanzhong, and S. Lukic, "ZCS LCC-compensated resonant inverter for inductive-power-transfer application," *IEEE Trans. Ind. Electron.*, vol. 58, no. 8, pp. 3500–3510, Aug. 2011.

[15] N. A. Keeling, G. A. Covic, and J. T. Boys, "A unity-power-factor IPT pickup for high-power applications," *IEEE Trans. Ind. Electron.*, vol. 57, no. 2, pp. 744–751, Feb. 2010.

[16] Y. Nagatsuka, N. Ehara, Y. Kaneko, S. Abe, and T. Yasuda, "Compact contactless power transfer system for electric vehicles," in *Proc. IPEC*, 2010, pp. 807–813.

[17] D. A. G. Pedder, A. D. Brown, and J. A. Skinner, "A contactless electrical energy transmission system," *IEEE Trans. Ind. Electron.*, vol. 46, no. 1, pp. 23–30, Feb. 1999.

[18] S. Krishnan *et al.*, "Frequency agile resonance-based wireless charging system for electric vehicles," in *Proc. IEVC*, 2012, pp. 1–4.

[19] B. T. Chuan, M. Kato, T. Imura, O. Sehoon, and Y. Hori, "Automated impedance matching system for robust wireless power transfer via magnetic resonance coupling," *IEEE Trans. Ind. Electron.*, vol. 60, no. 9, pp. 3689–3698, Sep. 2013.

[20] B. T. Chuan, T. Imura, M. Kato, and Y. Hori, "Basic study of improving efficiency of wireless power transfer via magnetic resonance coupling based on impedance matching," in *Proc. IEEE ISIE*, 2010, pp. 2011–2016.

[21] K. Van Schuylenbergh and R. Puers, *Inductive Powering: Basic Theory and Application to Biomedical Systems*. Dordrecht, The Netherlands: Springer-Verlag, 2009.

[22] J. Huh, S. W. Lee, W. Y. Lee, G. H. Cho, and C. T. Rim, "Narrow-width inductive power transfer system for online electrical vehicles," *IEEE Trans. Power Electron.*, vol. 26, no. 12, pp. 3666–3679, Dec. 2011.

[23] R. W. Erickson and D. Maksimovic, *Fundamentals of Power Electronics*, 2nd ed. New York, NY, USA: Academic, 2001.

[24] L. Bing, L. Wenduo, L. Yan, F. C. Lee, and J. D. Van Wyk, "Optimal design methodology for LLC resonant converter," in *Proc. 21st IEEE APEC Expo.*, 2006, pp. 533–538.

Siqi Li (M'09) received the B.S. and Ph.D. degrees in electrical engineering from Tsinghua University, Beijing, China, in 2004 and 2010, respectively.

From 2011 to 2013, he was a Postdoctoral Fellow with the University of Michigan, Dearborn, MI, USA. Since 2013, he has been with the Faculty of Electric Power Engineering, Kunming University of Science and Technology, Kunming, China, where he is currently a Lecturer with the Department of Electrical Engineering, as well as the Director of the Advanced Power Electronics and New Energy Laboratory. His research interests include battery management system and high-performance wired and wireless battery chargers for electric vehicles.

Weihan Li (S'13) received the B.S. degree in automotive engineering from Hefei University of Technology, Hefei, China, in 2010. He is currently working toward the Ph.D. degree in automotive engineering with Hefei University of Technology.

From September 2012 to August 2014, he has been a joint Ph.D. student funded by the China Scholarship Council with the GATE Center for Electric Drive Transportation, Department of Electrical and Computer Engineering, University of Michigan, Dearborn, MI, USA, where he is involved in the modeling and design of wireless charger for electric vehicles (EVs)/plug-in hybrid EVs. His research interests include wireless power transfer, EV/PHEV systems, renewable energy, and power electronics.

Junjun Deng (S'13) received the B.S. and M.S. degrees in electrical engineering from Northwestern Polytechnical University, Xi'an, China, in 2008 and 2011, respectively. He is currently working toward the Ph.D. degree in electrical engineering from the Northwestern Polytechnical University, Xi'an, China. He is a joint Ph.D. student founded by China Scholarship Council with the University of Michigan, Dearborn, MI, USA where he is involved in the modeling and design of ac/dc and dc/dc converters.

He is currently a Research Assistant with the Department of Electrical and Computer Engineering, University of Michigan. His research interests include resonant power conversion and high-performance battery chargers for electric vehicles.

Trong Duy Nguyen (M'13) was born in Binh Dinh, Vietnam. He received the B.Eng. and M.Eng. degrees from the Ho Chi Minh City University of Technology, Ho Chi Minh, Vietnam, and the Ph.D. degree from Nanyang Technological University, Singapore.

He is currently with the Department of Electrical and Computer Engineering, University of Michigan, Dearborn, MI, USA. His current research interests include electrical machine design and drives, electromagnetics, and electrical energy conversion systems.

Chunting Chris Mi (S'00–A'01–M'01–SM'03–F'12) received the B.S. and M.S. degrees from Northwestern Polytechnical University, Xi'an, China, and the Ph.D. degree from the University of Toronto, Toronto, ON, Canada, all in electrical engineering.

He is currently a Professor of electrical and computer engineering and the Director of the newly established GATE Center for Electric Drive Transportation, University of Michigan, Dearborn, MI, USA, founded by the U.S. Department of Energy. He has conducted extensive research and has published more than 100 journal papers. His research interests include electric drives, power electronics, electric machines, renewable energy systems, and electrical and hybrid vehicles.

Dr. Mi is a Distinguished Lecturer of the IEEE Vehicular Technology Society. He is also the General Co-Chair of the IEEE Workshop on Wireless Power Transfer sponsored by IEEE Power Electronics, Industrial Applications, Industrial Electronics, Vehicular Technology, Magnetics, and Power and Energy Societies. He is the Program Chair for the 2014 IEEE International Electric Vehicle Conference, the Chair for the IEEE Future Direction's Transportation Electrification Initiative e-Learning Committee, and a steering committee member of the IEEE Transportation Electrification Conference (ITEC-Asian). He serves as an Area Editor for the IEEE TRANSACTIONS ON VEHICULAR TECHNOLOGY and as an Associate Editor for IEEE TRANSACTIONS ON POWER ELECTRONICS and the IEEE TRANSACTIONS ON INDUSTRY APPLICATIONS. He was the Topic Chair for the 2011 IEEE International Future Energy Challenge and the General Chair for the 2013 IEEE International Future Energy Challenge.

He is a Guest Editor-in-Chief for the IEEE TRANSACTIONS ON POWER ELECTRONICS SPECIAL ISSUE on wireless power transfer and for the IEEE JOURNAL OF EMERGING AND SELECTED TOPICS IN POWER ELECTRONICS SPECIAL ISSUE on wireless power transfer.